Physical origins of optical anisotropy in quantum-confined semiconductors: the roles of valence band mixing, transition broadening and state filling

M. Lazarev[*]*, A. Rudra and E. Kapon*

Laboratory of Physics of Nanostructures Ecole Polytechnique Fédérale de Lausanne (EPFL), Switzerland

[*]*Present address: Department of Computer Science, LAMBDA, National Research University Higher School of Economics (HSE), Russia*

Abstract

We investigate experimentally and theoretically the impact of valence band mixing and spectrum of confined states on the polarization of light emitted from or absorbed by GaAs/AlGaAs semiconductor quantum dots (QDs) and quantum wires (QWRs) with tailored heterostructure potential. In particular, such nanostructures with parabolic-profile confinement potentials, realized by organometallic vapor phase epitaxy inside pyramidal pits, served as model systems for the study. Different degrees of linear polarization (DOLP) of emitted light, depending on the confinement potential profile, the specific excitonic transition and the level of excitation, are observed. A theoretical model shows that, besides the impact of valence band mixing, overlap of conduction and valence band wavefunctions as well as state occupation probability and broadening of transitions determine the DOLP. The conclusions are useful for the design of quantum light emitters with controlled polarization properties.

I. Introduction

Fundamentally, the polarization states of light emitted by direct-bandgap III-V semiconductors are related to the angular momentum of the valence band (VB) electronic states involved. Moreover, quantum confinement in heterostructures of lower dimensionality impacts the VB states and thereby can be employed to tailor their optical polarization properties. In typical, strain-free two-dimensional (2D) semiconductor quantum wells (QWs) excitonic emission proceeds via transitions between conduction band (CB) and VB states of pure heavy-hole (HH) or light-hole (LH) character [1], and the lower-energy HH states lead to optical absorption or emission with linear polarization vector lying in the QW plane [2]. On the other hand, 2D or 3D quantum confinement in quantum wire (QWR) or quantum dot (QD) structures induces VB mixing [3] even at the center of the Brillouin zone. This, in turn, modifies the polarization state of photons emitted by QWR or QD excitons, depending on the particular geometry of the confining heterostructure. In ideal QWR heterostructures, the lowest-energy radiative transitions are characterized by linear polarization oriented predominantly along the axis of the wire due to the LH character of the corresponding VB state [4]. In QD heterostructures, adding quantum confinement along the otherwise uniform-potential wire axis modifies the HH/LH admixture of the ground VB state, which can lead to switching of the polarization direction so as to direct it normal to the original wire axis [5]. Indeed, in strain-free, thin (i.e., height to width ratio smaller than one) QDs such as those prepared in the GaAs/AlGaAs system, the ground state (GS) excitons have predominantly

HH-like VB components [3], with corresponding emitted photons polarized in the weaker-confinement plane. However, in the case of thicker QDs the GS becomes LH-like, with linear polarization as in elongated QWRs [6]. Since QDs can serve as efficient emitters of single photons due to the full 3D confinement of the charge carriers [7],understanding the relationship between the geometry of the confining potential and light polarization can yield useful designs for emitters of single photons with controlled polarization states.

The relationship between the confinement geometry and valence band mixing and light polarization has been investigated for a variety of experimental QWR and QD configurations, including Stranski-Krastanow dots [8] and posts [9][10], V-grooved QWRs [11], and T-shape QWRs [12][13]. A particularly interesting QWR/QD configuration is offered by GaAs/AlGaAs heterostructures grown in inverted pyramids [14][15]. In this system, the QWR/QD heterostructures are self-formed along the growth direction, rather than in the plane of the wafer, due to strong Al-Ga segregation effects [16]. This allows the formation of vertical QWR-like structures of tight 2D confinement potential normal to the QWR axis, on which a modulation in the confinement potential with nm-precision can be superposed by changing the material composition along the growth direction [17]. In this way, a large variety of modulated–QWR and QD structures were realized, including QWRs of finite lengths [18], QDs with tailored potential profiles [17] and QD-in-QD [19] or QD-in-QWR [20] structures. The resulting modulated-potential QWR/QD structures permit the introduction of precise modification in the 3D-confinement potential and, in principle, tailoring of the VB-mixing effect and with it the polarization properties. Indeed, the expected polarization features of an ideal (infinitely long) QWR and of thin QDs were recovered using this model system [15].

In the present paper, we employ several AlGaAs pyramidal QWR/QD heterostructures in order to investigate the relationship between the 3D quantum confinement and the optical polarization properties. Since the degree of quantum confinement along the otherwise uniform potential of a QWR should have a direct effect on the VB mixing and hence the polarization features, we use in particular QDs made of a vertical pyramidal QWR in which a parabolic variation in the 2D confinement potential is introduced. By investigating several such parabolic-potential QDs (PQDs) with systematic increase in the potential gradient, we are able to gradually change the 3D confinement from a QWR-like configuration to a rather tight QD configuration, so that switching from a QWR-like to a QD-like behavior can be traced. Additionally, we investigate "long" QWR and "thin" QD structures that serve as reference structures. In this way, we can track the evolution of the optical polarization features from a 1D-like to a 0D-like structure made in the same experimental model system.

Figure 1 shows schematically the three groups of structures investigated here. Each region in the inverted pyramid has a different Al content, represented by different colors. The lowest Al-content values correspond to the QWR, thin QD or parabolic QD (QD) cores (orange color). The vertical confinements are accomplished by higher-bandgap (higher Al content) QWR barriers. Lateral confinement along the pyramid wedges is obtained by patterned vertical QWs (PQWs) (green color) or lateral QWRs (LQWRs)of intermediate Al-content and vicinal vertical QWs (PQWs) (blue color) or vicinal lateral QWRs (LQWRs) of relatively high AL content. The different Al contents in the same grown AlGaAs layer are achieved via different levels of Al-Ga segregation on the curved surfaces [16]. Comparing the measurements with numerical calculations of a theoretical model of the pyramidal heterostructures, we are able to elucidate the role of VB mixing

in determining the experimentally-observed polarization features. We conclude that, in addition to VB-mixing effects, overlap of conduction and valence band wavefunctions as well as state occupation probability and broadening of the transitions have important roles in explaining the observations.

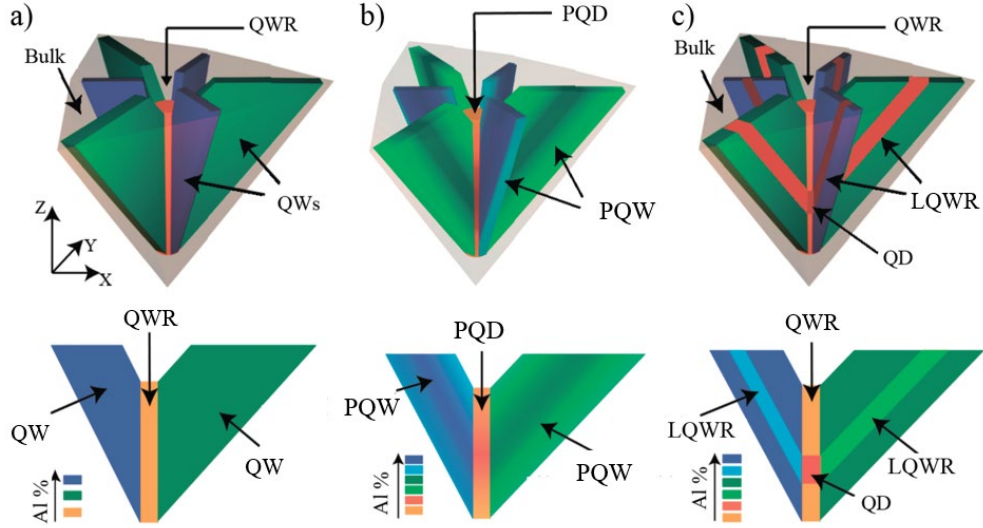

Figure 1. Schematic illustration of different kinds of AlGaAs nanostructures embedded in inverted pyramids presented in this paper. (a) "Long" quantum wire (QWR) laterally bounded by "vertical" QWs, (b) parabolic potential quantum dot (PQD), and (c) QD-in-QWR heterostructure. The upper panel shows the full 3D structures whereas the lower panel displays cross-sectional views through the center of the structures. The color codes scale the Al mole fraction in the different parties of the heterostructures.

II. Experimental: QD/QWR fabrication, structure and measurement set up

The fabrication of the nanostructures in the inverted pyramids is an example of site-controlled nanostructure formation. The sites and maximum nanostructure size are defined by pattern. The approach is similar as for V-grooved QWRs made on patterned (100) substrates [10], but in this case a (111)B substrate is patterned with inverted tetrahedral pyramids limited by (111)A facets. Patterning consists of a photolithography step using reactive ion etching (RIE), that first creates an array of holes in a SiO_2 (or SiN) layer deposited on the (111)B GaAs substrate, as shown in Fig. 2(c). The hole-size in the SiO_2 layer determines the size of inverted pyramid. Pattern transfer into the substrate is performed by wet chemical etching in 1% Br-Methanol solution, resulting in a regular array of inverted tetrahedral pyramids (see Fig. 2 (d)).

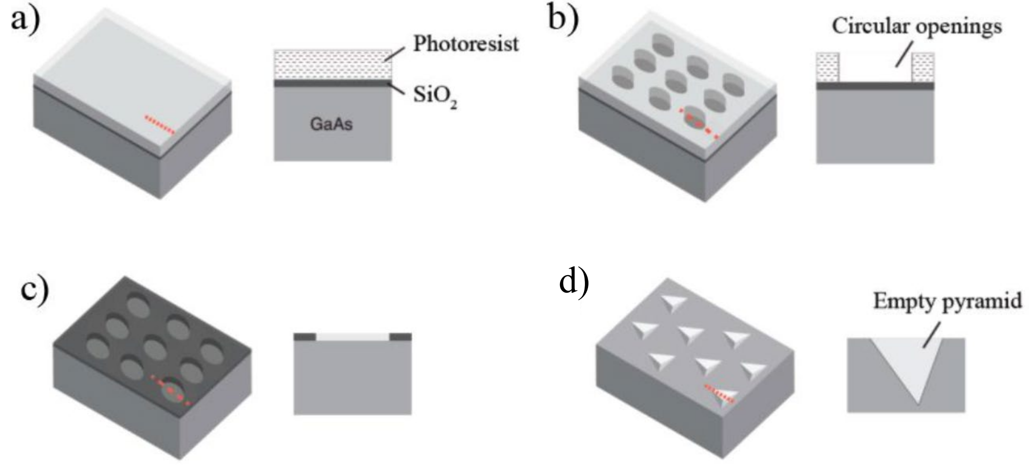

Figure 2 Schematic illustration of the substrate patterning process and its schematic cross-sections (a,b,c,d). a) The substrate after SiO_2 and photoresist deposition; b) the substrate after photolithography step; c) pattern after RIE and photoresist removal; d) schematic illustration of the patterned pyramids after wet etching and SiO_2 removal. Adapted from [21]

Next, the QD/QWR nanostructure is self-formed inside the pyramids during metalorganic vapor phase epitaxy (MOVPE) of specific GaAs/AlGaAs heterostructures [22]. Particular features of this approach is the self-limiting formation of a sharp (~10nm wide) corner at the bottom of each pyramid, and strong Al-Ga segregation resulting in Ga-enriched AlGaAs alloys at the sharp edges of the pattern [23]. This permits the formation of a low-bandgap AlGaAs QWR at the center of the pyramid, laterally confined by higher bandgap QW regions oriented along the three wedges of the pyramid and still-higher bandgap AlGaAs bulk in the remaining vicinity (see Fig. 1(a)). The effective Al contents at the QWR and these side-QWs are reduced by factors of ~6 and ~2, respectively, with respect to the corresponding bulk values [24].

The length of the VQWR can be fixed with nm precision by controlling the vertical growth of the heterostructure involved [3]. More relevant to the study presented here, growing a QWR heterostructure in which the Al-content is deliberately varied along its axis makes possible the formation of a variety of 1D-0D nanostructures with controlled energy states. Imposing a parabolic profile on the Al content gives rise to a parabolic QD (PQD) core, in which the gradient of the profile determines the separation of the confined QD states. The QWs grown at the wedges of the pyramid are then transformed into parabolic QW (PQW) structures, as shown schematically in Fig. 1(b). Finally, replacing the QWR core by a thin GaAs layer results in the formation of a few-nm thick GaAs QDs at the bottom of the pyramid, embedded in QWR segments vertically and lateral QWR (LQWR) structures along the pyramid wedges, as well as bulk AlGaAs regions (see Fig. 1(c)).

A particular set of pyramidal nanostructures was designed and prepared in order to explore in a systematic way the evolution of optical polarization properties in systems of dimensionality between one and zero. The design of the structures is based on a simplified model of the effective Al-content resulting from the capillarity-driven Al-Ga segregation at the sharp bottom and three wedges of the inverted pyramids [22]. The (lower) Al content at the sharp corners can be written:

$$x_{eff} = \frac{x}{x + K(1-x)} \quad (1)$$

where x is the nominal (bulk) Al concentration of the grown alloy. In previous studies, it was found that $K=8.9$ for central QWR and $K=2.1$ for side QWs and LQWRs [25]. This "effective" Al content x_{eff} permits to calculate the bandgap of the corresponding components of the 3D pyramidal heterostructure, as discussed below.

All samples studied here were produced by growing the specific set of layers reported in Table I on 2°-off-(111)B GaAs substrates patterned with tetrahedral pyramid pits. Other growth parameters used can be found in [24][26]. The etch-stop layer introduced after the "ramp" layer was used for back etching of the substrate in order to facilitate top-side optical spectroscopy. The nominal Al contents translated into local AlGaAs compositions (and bandgaps) in the different parts of the pyramids, as described above, thus fixing the heterostructure potential distribution. Among the set of samples used, only the size of the QWR/QD cores was varied in order to realize the specific low-dimensional structures further investigated. Table II presents the parameters of the five different samples grown.

Layer	**Material**	**Al content (%)**	**Nominal thickness (nm)**	**Susceptor Temperature (°C)**
Buffer	GaAs	0	10	735
Ramp	AlGaAs	30-75	10	>770
Etch-stop	AlGaAs	75	45	770
Lower barrier	AlGaAs	40	100	705
QD/QWR core	*	*	*	*
Upper barrier	AlGaAs	40	45	705
Cap	GaAs	0	5	705

Table I. Layer structure of the samples studied, starting from the initial buffer layer up to the top cap layer. Al content and thicknesses correspond to those resulting for planar growth on (100) GaAs wafers. Al layers are nominally undoped.

Structure core part name and (actual thickness)	**Material**	**Al content**	**Nominal thickness (nm)**	**Susceptor temperature T (C)**
QD (5 nm)	*GaAs*	*0*	*1*	*705*
QWR (480 nm)	*AlGaAs*	*20*	*240*	*705*
PQD-120 (nm)	*AlGaAs*	*40-20-40*	*60*	*705*
PQD-240 (nm)	*AlGaAs*	*40-20-40*	*120*	*705*
PQD-480 (nm)	*AlGaAs*	*40-20-40*	*240*	*705*

Table II. Growth parameters of the different QD/QWR core nanostructures parts produced in the present study. The Al contents for the PQD structures refer to the values at the two extremities and

center of the parabolic composition variation. The actual thickness of each structure are indicated in parenthesis.

Scanning electron microscope (SEM) images of one of the samples after growth (QWR sample) is shown in Fig. 3. The pyramids had typically ~4.5 µm long sides and were arranged in arrays of 5 µm pitch (see Fig. 3 (a)). After MOVPE growth, the surface of the sample was preferentially wet-etched in order to remove parasitic growth; a top-side image of a grown pyramid after such etching is shown in Fig. 3(b). Better access to the nanostructure core during optical characterization was permitted by removing the GaAs substrate [27]; an image of a grown pyramid (from the bottom side) is depicted in Fig. 3(c).

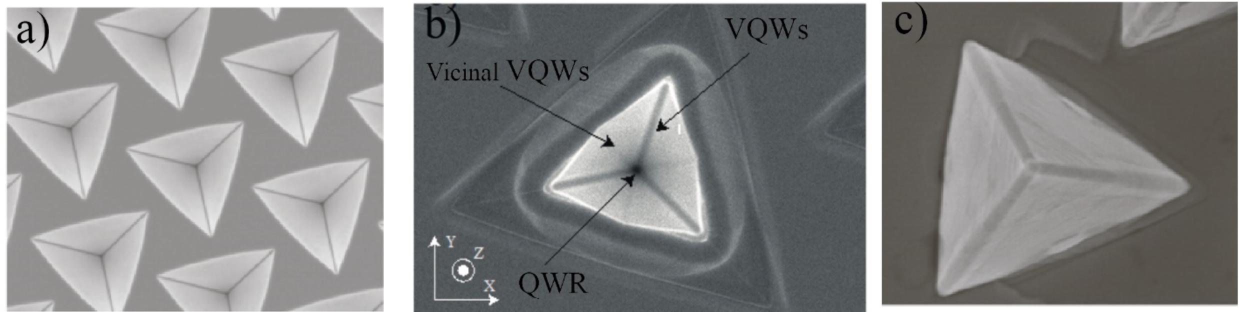

Figure 3. SEM pictures of QWR sample (a) SEM top-view image on patterned sample surface before the growth. (b) SEM image of pyramid after the growth and surface etching. (c) SEM picture of a single back-etched pyramid.

Experimental analysis of the optical properties of the grown nanostructures included measurements of the polarization features of the photoluminescence (PL), which required access to the core of the pyramids in side-view. This was accomplished by cleaving the pyramidal structures along the [112] crystallographic direction, as shown in Fig. 4. The cleaved sample was then placed in a He-flow cryostat, and was excited by a 532 nm wavelength laser beam focused to a 1-2µm spot using a 50X microscope objective lens. The PL was collected along the [110] direction using the same objective lens and analyzed using a grating spectrometer coupled to a liquid-nitrogen cooled Si CCD, with a spectral resolution of about 80 µeV.

In particular, the intensity of particular lines was resolved in linear polarization, yielding the polarized emission intensities I_z and I_{xy}, polarized along the vertical direction (V) and horizontal direction (H) (see Fig. 4), from which the degree of linear polarization (DOLP)

$DOLP = \frac{I_z - I_{xy}}{I_z + I_{xy}}$ was derived.

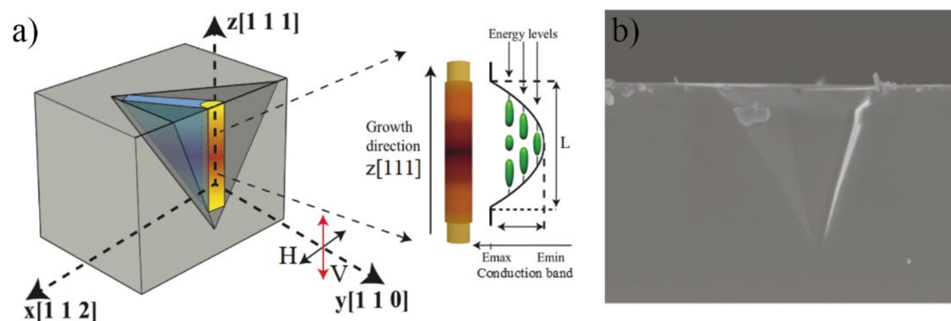

Figure 4. Schematic crossection of tailored potential nanosrutcure in inverted pyramid (planarized for illustration simplicity) with indicated axes. (b) SEM picture of the cleaved inverted pyramid after growth (the structure is typically not fully planarized).

Figure 4 also shows a schematic representation of the confining heterostructure potential in the conduction band for a PQD structure, along with several (calculated) confined envelope function of electrons in the conduction band. The depicted length L of the PQD heterostructure, measured along the growth direction, is indicated in Table I for the set of experimental samples investigated.

III. Model of confined states and optical spectra

Modelling of the conduction band (CB) and valence band (VB) states in the different samples was based on a simplified configuration accounting for the important features of the actual pyramidal nanostructure. The QWR structure was modeled as a cylinder of diameter D_{in}=20nm [25]. The length of these cylinders (and all other vertical dimensions) was set to twice the nominal thickness of the grown structure (for the PQD and QWR samples), based on calibrations of growth rates inside the pyramid. The vertical structure and its CB and VB edges are schematically depicted in Fig. 5. The three lateral VQWs forming the lateral barriers were modeled as 15nm thick slabs, arranged along the three major wedges of the pyramid, with effective Al content derived from the reduced segregation effect at the V-groove wedges (see eq. (1)). The “vicinal” VQWs shown in Fig. 3 (b) were ignored because of the very small segregation effect at their cores [28].

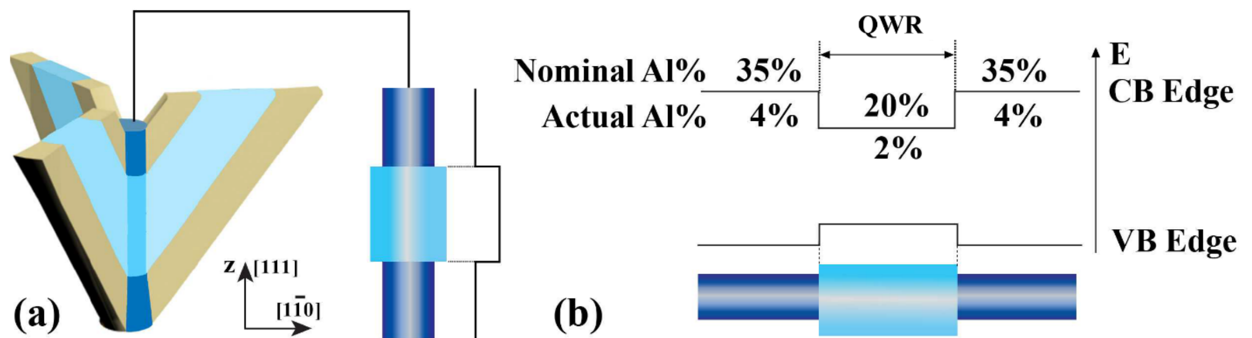

Figure 5. Schematic description of the model of the pyramidal nanostructure used for modelling the confined carrier; (a) Simplified pyramidal nanostructure configuration showing the profile of the Al content along the growth axis; (b) schematic distribution of Al content along the QWR and corresponding CB and VB edges.

In the model for the parabolic PQDs, the nominal Al content was varied parabolically, from $x=0.2$ at the center of the core to $x=0.4$ at each barrier, in a symmetric way, in order to simulate the actual growth parameters of the corresponding samples. The actual Al content was determined such as to reflect the Al-Ga segregation effect. The parabolic x-variations indices confinement along the QWR axis, yielding QD potential wells of a profile that tailored with great (~1 nm) precision. The central nanostructure geometry is also known to be a cylinder-like with diameter of 18-20nm for long (>20nm) structures [18]. In the case of small structures due to segregation processes it tends to have lens shape [29] An example of the actual (computed) Al content profile along the center of the modulated QWR is shown in Fig. 6 (center panel) for PQD-120nm sample (nominal L=60nm). Two-dimensional cross-sections of the actual Al contents in PQD 120nm sample, both along and across the core, are shown in Fig. 6. Note that in these PQD structures, the side-VQW

barriers become VQWs with parabolically shaped potentials across their axis, which is properly taken into account by the model as well.

After setting the 3D Al content distribution across the pyramidal nanostructure, the corresponding bandgap and CB/VB edges were determined following the local AlGaAs composition. The semiconductor bandgap and band edges were estimated using well-known expression for $Al_xGa_{(1-x)}As$ compounds [30]:

$$E_g\left(Al_xGa_{1-x}As\right)=\left(1-x\right)E_g\left(GaAs\right)+xE_g\left(AlAs\right)-x\left(1-x\right)C\,.$$

where C is the bowing parameter, $E_g(GaAs)$= 1.519 eV and $E_g(AlAs)$= 3.1 eV (low temperature values). The ratio between the CB and VB offsets was taken as ΔCB/ ΔVB ~67/33 [31][32]. The confined energy states in the CB and the VB were determined by numerically solving Schroedinger's equation in a 30x30x300nm^3 volume (XxYxZ, see Fig. 4(a)). As it was pointed above the segregated Al content is not the same in all pyramid regions. From the previous study we know ratio of effective Al content Balk/QWs (side) and Balk/QWR (center). [33]. Thus, we can estimate confinement potential profile in the nanostructure.

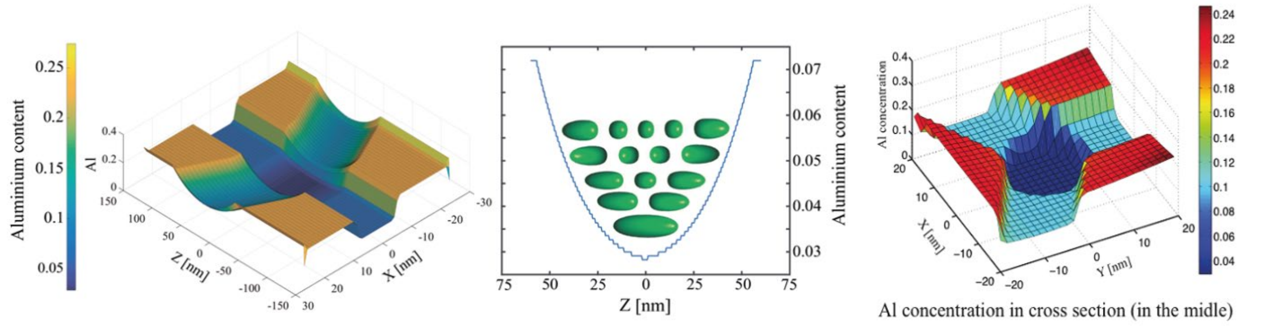

Figure 6. Modeled effective Al content profile of the PQD-120nm structure. Left: 3D plot of (actual) Al content in XZ plane (along the growth direction); right: profile at QD center in horizontal plane (XY). Calculated confined electron WFs inside the QD depicted in green color. (Note: WF energy position does not represent the actual corresponding energy).

To compute the band structures, we use a model based on ***k.p*** approximation [34] and Lowdin's perturbation [35], eventually leading to the formulation based on the Luttinger Hamiltonian [36] [37]. Details of the numerical model are given in. In particular, the impact of the VB structure on the polarization of the emitted light is set by the VB wavefunction, cast in the framework of a 4X4 Luttinger Hamiltonian model for a GaAs-based compound semiconductor [39]. The valence band wave function can be presented as:

$$\varphi_{vb}=\varphi_{HH\uparrow}\left|\frac{3}{2};\frac{3}{2}\right\rangle+\varphi_{LH\uparrow}\left|\frac{3}{2};\frac{1}{2}\right\rangle+\varphi_{LH\downarrow}\left|\frac{3}{2};-\frac{1}{2}\right\rangle+\varphi_{HH\downarrow}\left|\frac{3}{2};-\frac{3}{2}\right\rangle$$

where $\left|l,m\right\rangle$ *3/2, 1/2*,

respectively, arrows indicate spin directions, and $\varphi_{HH\uparrow},\varphi_{LH\uparrow},\varphi_{LH\downarrow},\varphi_{HH\downarrow}$ are the corresponding envelope wavefunctions. The rate of a radiative transition from a CB state to a VB state, resolved in linear polarization along *z* and *x-y* (see Fig. 3 (a)) is proportional to $\left\langle\varphi_{cb}\left|\hat{e}\bullet\vec{p}\right|\varphi_{vb}\right\rangle$ where $\vec{p}$

is the momentum and $\hat{e}$ denotes the polarization direction. This gives the corresponding polarization-resolved light intensity components:

$$I_z \propto \frac{4}{3}\langle\varphi_e|\varphi_{LH}\rangle^2 \qquad\qquad I_{xy} \propto \langle\varphi_e|\varphi_{HH}\rangle^2 + \frac{1}{3}\langle\varphi_e|\varphi_{LH}\rangle^2 \tag{2}$$

Where $|\varphi_{LH}\rangle = |\varphi_{LH\uparrow}\rangle + |\varphi_{LH\downarrow}\rangle$ and $|\varphi_{HH}\rangle = |\varphi_{HH\uparrow}\rangle + |\varphi_{HH\downarrow}\rangle$ hence the DOLP reads

$$DOLP = \frac{\langle\varphi_e|\varphi_{LH}\rangle^2 - \langle\varphi_e|\varphi_{HH}\rangle^2}{\frac{5}{3}\langle\varphi_e|\varphi_{LH}\rangle^2 + \langle\varphi_e|\varphi_{HH}\rangle^2}$$

For VB states with pure HH character this yields *DOLP = -1* whereas for pure LH states it gives *DOLP = 0.6*. These values correspond to the ideal cases of thin QD and infinitely-long QWR, respectively. In intermediate cases of quantum confinement, studied in the present article, mixing in the HH/LH character of the VB states is expected leading to intermediate values of the DOLP.

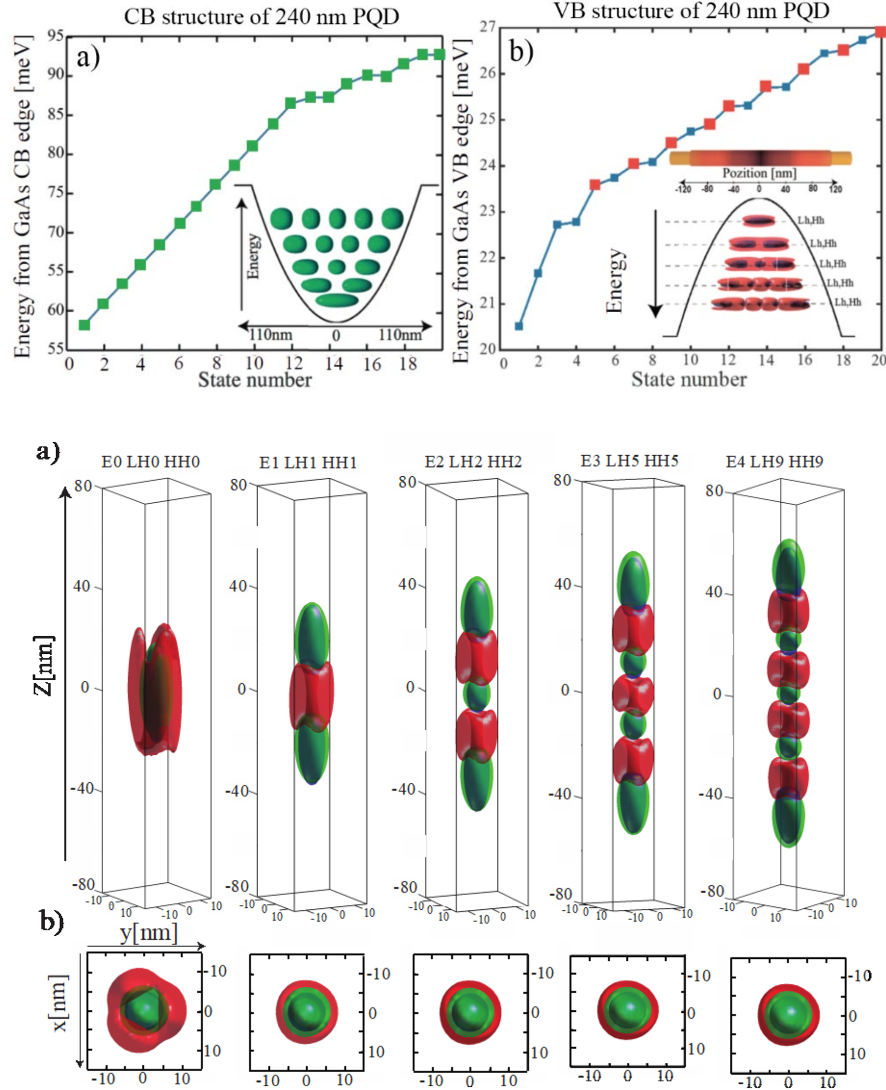

Figure 7. CB and VB structure calculated for the PQD 240nm sample. Upper panel: state energies and envelope wavefunctions for (a) the CB and (b) the VB. Insets show several low-energy

wavefunctions. Lower panel: 3D distribution of the envelope functions in the Z-Y (upper part) and X-Y (lower part) planes, for several (strongest transition), lower-energy states. Color codes: green-CB states, blue-dominant LH state, red- dominant HH state. Note that the LH parts of the wavefunctions in the lower panels are mostly hidden by the electron wavefunction parts.

We first consider the case of the PQD-240nm sample, which represents a case of an elongated, QWR-like structure of finite length, in which VB mixing effects are significant. The calculated band structure for the PQD-240nm sample is presented in Fig. 7. The energies (labeled by En, HHn and LHn for electron, predominantly-HH and predominantly-LH states) and envelope wavefunctions of the strongest-transition states are illustrated. The first ~10 electron states are equally spaced, consistent with the truncated -parabola confinement potential (Fig. 7(a)). The VB structure is more complex and consists of LH-like and HH-like mixed states. Only the first 3 lowest-energy states are equally spaced (figure 7 (b)) with dominant LH WF part (blue squares), whereas higher-energy states acquire strong HH character (red squares). Note, however, that even the lowest energy, predominantly-HH states, have some parts of the wavefunctions displaying a LH-character. Remarkably, the LH-parts of the wavefunctions are localized at the core of the PQD, similar to the electron wavefunctions, whereas the HH-parts are located further out on the periphery of the core.

The lower panel in Fig. 7 shows the 3D wavefunction distributions of the CB and VB states with the strongest transition rates (i.e. the largest overlaps of the CB and VB envelope functions). The probability density of the CB-wavefunction isosurface (green) $\langle \varphi_e | \varphi_e \rangle^2$ is 5.10^{-5}, for the LH-wavefunction (blue) $\langle \varphi_{LH} | \varphi_{LH} \rangle^2$ it is 5.10^{-6}, and for the HH-wavefunction (red) $\langle \varphi_{HH} | \varphi_{HH} \rangle^2$ it is 5.10^{-7}. From this figure, one can see (qualitatively) that transitions involving the depicted states are dominated by the overlaps of the electron and LH-components of the envelope functions, like in infinitely long QWRs. However, increasingly large overlap with the HH-components occurs for higher energy states.

The role of the overlap of the different wavefunction components on the DOLP spectra is investigated theoretically in more detail in Fig. 8, for sample PQD-240nm. This figure depicts the transition rate intensity as defined in (2) and (3), which represents the relative optical absorption rates corresponding to transition between the various CB and VB states as calculated above. First, Fig. 8(a) shows the squared overlaps between the electron and LH or HH components of the wavefinctions, which are later used in (2) to calculate the relative intensities I_z and I_{xy}. The major transition rates at the considered photon energy range are dominated by the LH components of the CB states. Weak contributions from the HH components appear at higher energies due to the more complex geometries of the higher-order wavefunctions.

Using these wavefunction overlaps, the normalized absorption rates were then calculated according to (2). The result, accounting for energy broadening of 2.5meV due to possible charge fluctuations around the nanostructure, and including carrier-carrier Coulomb interaction in a perturbative calculation [40], is depicted in Fig. 8(b). Note that the Coulomb interaction results in red shifts of the different state energies. Clearly, the absorption spectrum is dominated by the parallel polarization component related to the LH-components of the CB states. However, this dominance is reduced for the higher energy transitions due to the contributions of the overlaps with the HH wavefunctions already shown in Fig. 8(a). The DOLP spectrum, derived from Fig.

8(b) via (3) permits to estimate quantitatively the impact of the line broadening on the deviation from pure LH-like transitions in this case. For the lowest energy transition, the absence of contributions of HH overlaps near the main LH-related transition renders the value of the DOLP very close to 0.6, as expected for a pure LH-like transition. On the other hand, the line broadening is responsible from the significant decrease in the DOLP from the 0.6 value for the higher energy transitions, a direct manifestation of line broadening and superposition of HH-like overlaps. As further shown in Fig. 8(d), increasing line broadening systematically reduces the DOLP of the higher energy main absorption peaks, as more and more HH-components superpose.

This case of weak confinement along an otherwise infinitely-long QWR illustrates the roles of wavefunction overlaps and state broadening on the DOLP of the optical absorption spectra. The lowest-energy transitions are dominated by the LH-parts of the wavefunctions due to the better overlap of those parts with the electron (CB) wavefunctions. This brings about the positive values of the DOLP peaks. However, line broadening result in superposition of the HH-like transitions, which reduces the peaks of the DOLP from the 0.6 value in the absence of confinement along the QWR axis.

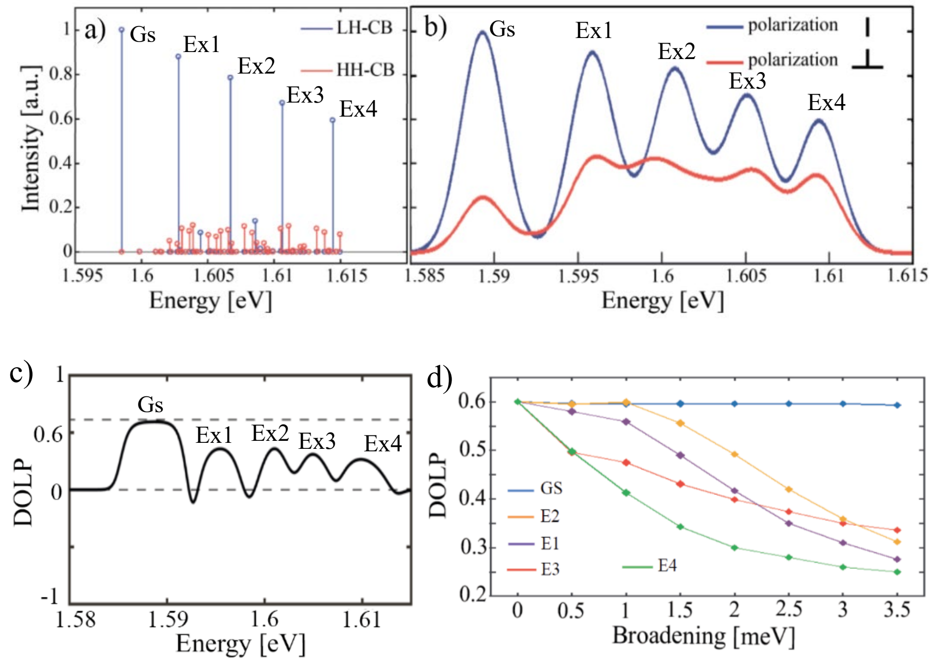

Figure 8. Calculated (relative) optical transition rates in sample PQD-240nm. (a) Calculated absorption rate components versus photon energy, without line broadening. Blue and red colors correspond to rates involving light and heavy holes, respectively. (b) Corresponding absorption spectra resolved in polarization, with broadening (2.5 meV) and including coulomb interaction redshift as a perturbation. Red and blue curves correspond the convention in Fig 4. (c) Calculated DOLP, derived from (c). (d) Values of the DOLP peaks versus line broadening.

In order to examine in more detail, the increasing effect of confinement along the QWR axis, we compare in Fig. 9 the calculated optical spectra of all samples studied in the present work (see Tables I and II for details on structures). Figure 9 (a) considers the two extreme cases of long QWR and thin QD. In the QWR (of finite length) case, the transitions are completely dominated by the LH-character of the VB states. Note that the discreet energies of the states involved are related to the finite length (480nm) of the QWR. Their separations conform to the 1D density of states

spectrum that would take place as the wire lengths increases indefinitely. The LH-character in this case is also well reflected the calculated absorption spectra (including broadening and Coulomb interaction) that exhibit linear polarization oriented mainly along the QWR axis, with DOLP~0 at its peak.

In the case of the thin-QD, the ground state transition is completely dominated by the HH-character of the CB state involved, with linear polarization of the corresponding absorption peak oriented perpendicular to the growth axis (DOLP=-1). However, the transitions related to excited states with LH-character show DOLP~0.6, as for typical ground state QWR transitions.

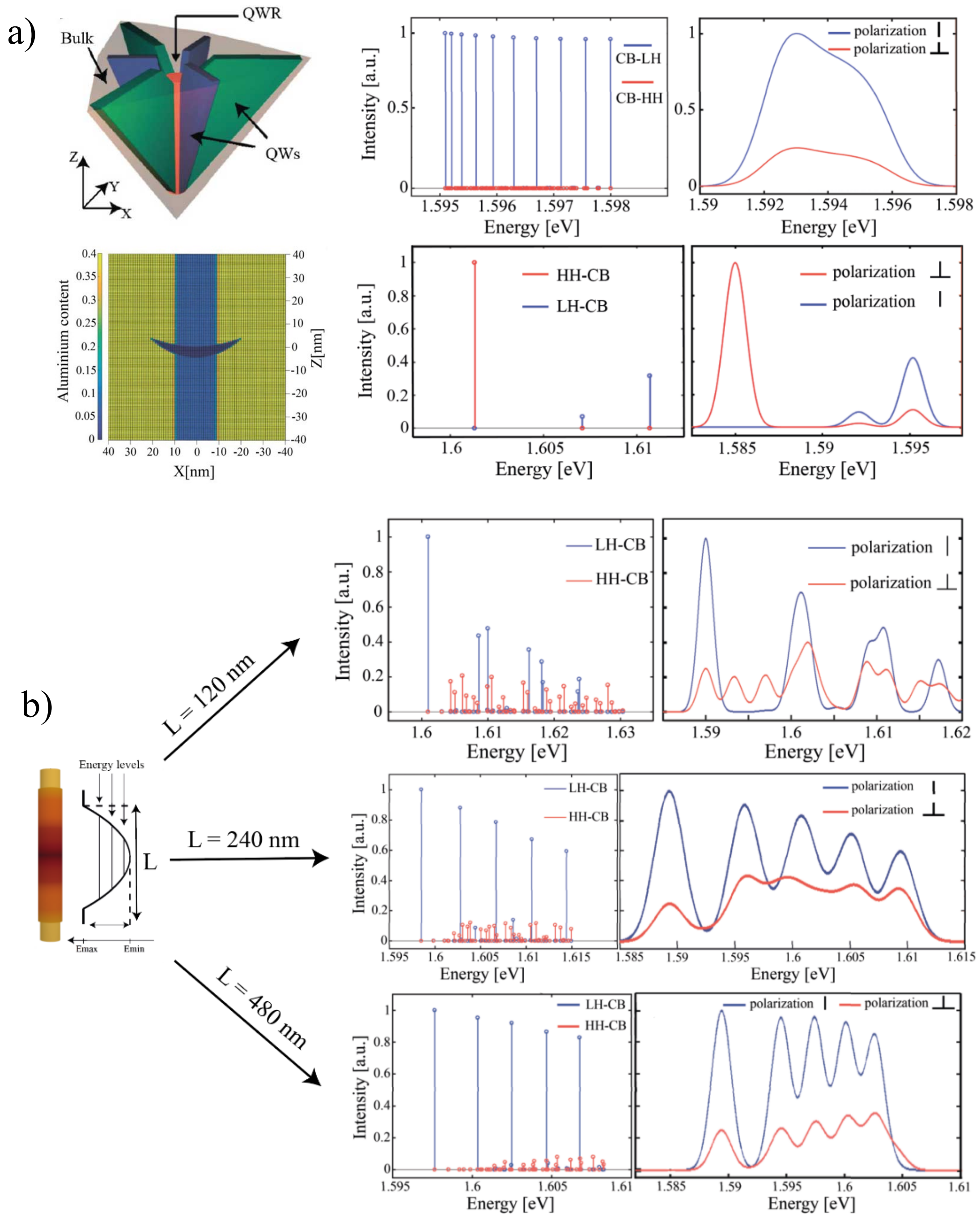

Figure 9. Comparison of the calculated optical spectra of the studied nanostructures. Schematics on the left show the structure of the QWR, QD and PQDs considered. The left columns show the calculated LH and HH components of the transition rates. Right columns show the calculated

relative absorption rates resolved in polarization (along and perpendicular to the main axis), including line broadening (2.5 meV) and coulomb interaction. (a) QWR structure (top) and thin QD structure (bottom). (b) PQD structures, from top to bottom: samples PQD-120nm, 240nm, 480nm.

Comparing the calculated spectra of the three PQD samples (Fig. 9(b)), we observe that they exhibit features intermediate between the extreme case of thin QD and "long" QWR. In all cases, the elongated shape of the 3D potential well yields a ground state absorption feature very similar to that of an infinitely long QWR, with DOLP=0.6 at the peak of the transition. With increasing confinement in the growth directions, more and more transitions with stronger HH-character appear, as a result of the VB mixing. Moreover, due to the finite linewidths, these transitions overlap the LH-related ones, and reduce the value of the DOLP below 0.6. With significant confinement, absorption peaks with DOLP=-1 eventually appear.

IV. Measured optical spectra

Before acquiring and analyzing the polarization-resolved PL spectra of the series of samples, PL spectra were measured in a wide photon energy range for back-etched samples, with excitation and collection of the light from the top side of the pyramids. In this configuration, emissions from all different parts of the pyramidal nanostructures could be easily observed, permitting the identification of transitions due to recombination in the core QWR or QD structures of interest.

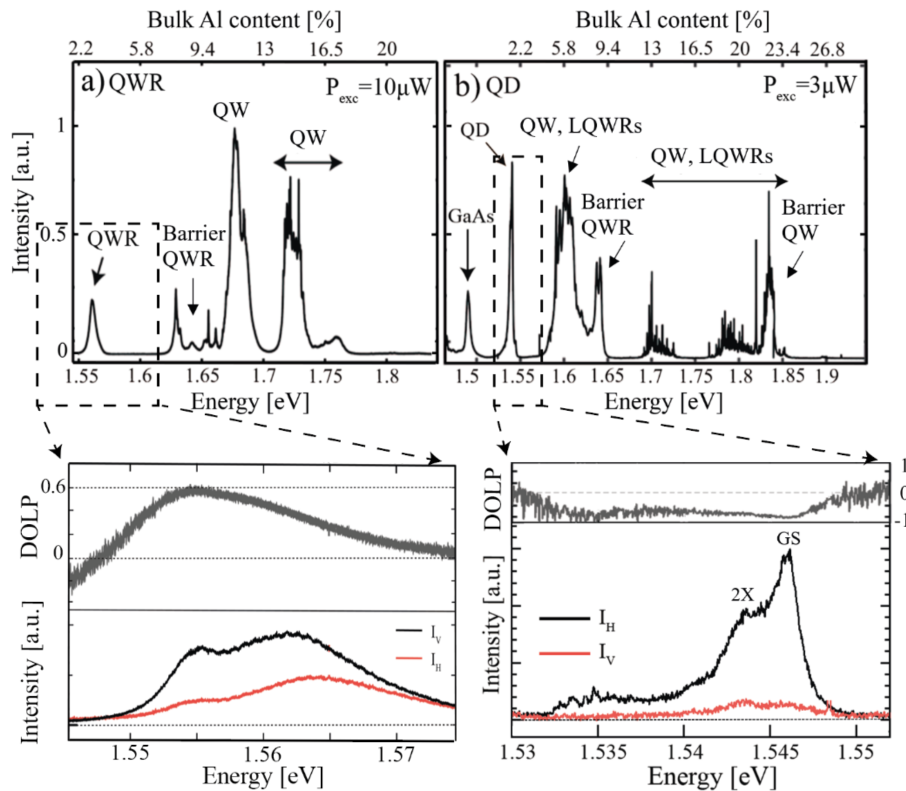

Figure 10. PL spectra collected from the top of back-etched pyramids (upper panels) and polarization-resolved PL with corresponding DOLP spectra acquired in side-view (lower panels) for (a) the 480nm long QWR sample and (b) the thin QD sample (T=10K).

Figure 10 shows the results of this approach for the QWR and QD structures. Excited at relatively high light intensity, the top-view PL spectra show emission from the low energy cores as well as the higher energy barriers due to the high carrier density produced. Along the photon energy scale, the Al content of an AlGaAs alloy that would emit photons of the same energy is also depicted. Based on the effective bandgaps and the Al content of the equivalent AlGaAs alloy, estimated from the structural studies, the different PL lines can be identified. For the QWR sample, the lines at 1.56eV and around ~1.64eV are assigned to the strongly segregated vertical QWRs formed at the core layer and the vertical barrier layers. Similarly, the lines at ~1.66eV and ~1.725 eV are due to emission from the less segregated QWs grown at the pyramid wedges within the core layer and the vertical barriers, respectively. The GaAs-QD line at ~1.545eV as well as PL from the vertical AlGaAs QWR barrier at ~1.64 eV is identified. PL from the GaAs QD layer that form the LQWRs along the pyramid wedges and the QW layers on the pyramid facets are seen around ~1.6eV. The higher energy lines from ~1.7 to ~1.85 emanate from the wedge, facet and bulk of the barrier AlGaAs layer.

Focusing on the lowest energy lines originating from the core QWR and QD parts, side-view, polarization-resolved PL spectra were acquired at higher excitation intensities of 300 μW for the QWR and 50 μW for the QD samples in order to better resolve spectrally the different excitonic recombination lines. The DOLP spectra are very similar to the calculated results of Fig. 9(a), with DOLP values of 0.6 for the QWR peak and -1 for the QD line. For the QD structure, 2X recombination as well as multi-exciton features can be observed in addition to the X GS line.

Figure 11 displays the measured side-view PL spectra, resolved in linear polarization, for a parabolic QD structure of L=240 nm at several levels of excitation (T=10 K). Several transitions appear as peaks in the PL spectra, with a ground state (GS) transition dominating at low powers and additional bi-exciton (2X) and excited state (Ex n) transitions appearing due to state filling. The regular spacing of the transitions (~4 meV) is a manifestation of the parabolic potential profile of the QD. Similar spectra were observed for the other samples, with L=120 nm and 480 nm, but with different energy spacing of the observed transitions (~8 meV and ~2 meV, respectively).

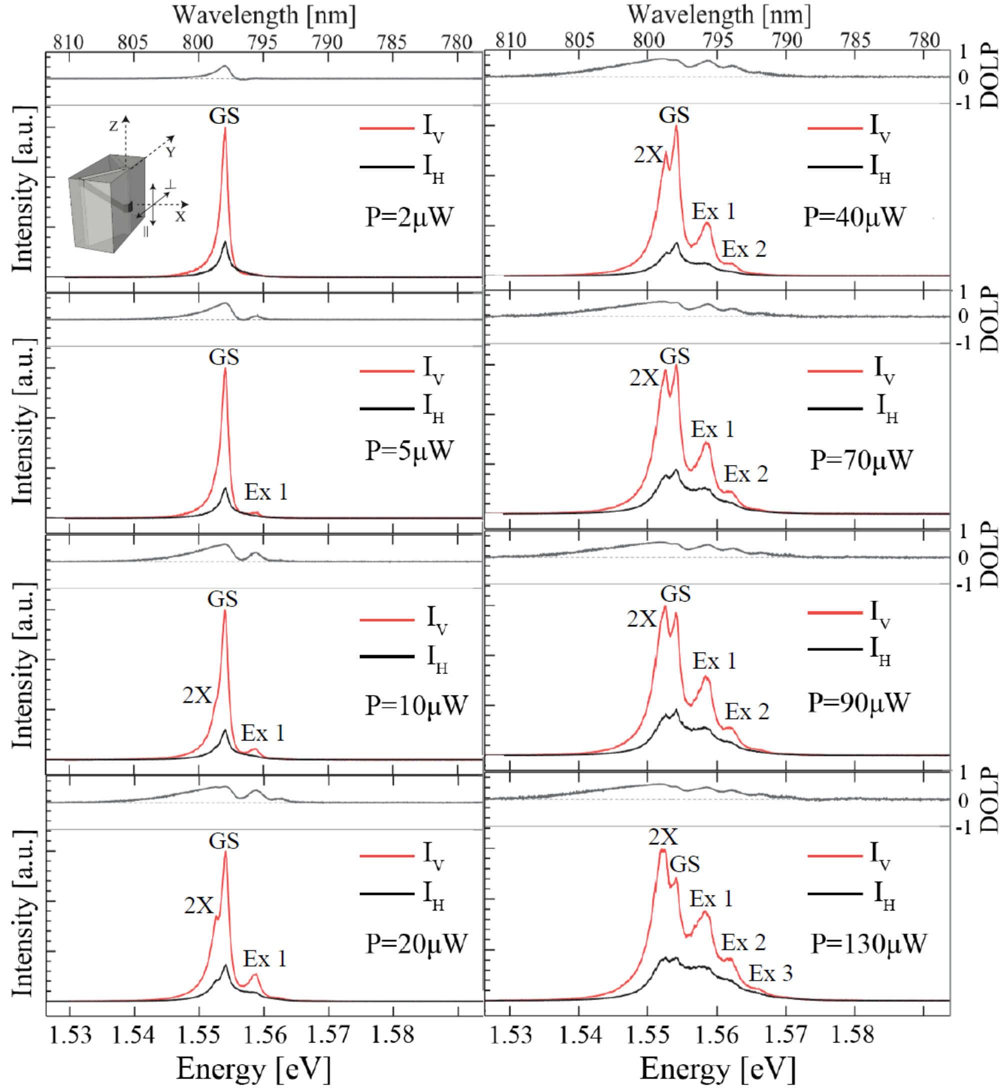

Figure 11. Polarization resolved PL spectra (lower panels) and DOLP spectra (upper panels) for a PQD-240 nm) at T=10 K and at different excitation levels P. Vertical (V) and horizontal (H) polarization components correspond to the convention in fig 4 (a).

Experimentally, both the ground state and the excited state transitions show dominant V-polarized emission, with the Gs X transition exhibiting DOLP=0.6 right from lowest excitations, consistent with the simulated data. On the other hand, the excited state transitions show lower values of DOLP. This is an indication that state filling effects are also significant for explaining the polarized emission behavior in such structures, as further discussed in what follows.

V. Origins of polarization anisotropy evolution.

Excitonic systems in quantum nanostructures, excited by optical or electrical pumping, are not in thermal equilibrium. However, relaxation and scattering processes in each band (CB or VB) are much faster than the interband recombination rates. Exciton lifetime (that corresponds to interband transitions between charged carriers) in such systems is typically more than 100 ps which is higher by orders of magnitudes than intraband transition in CB or VB that are dominated by charge carrier scattering [41]. This leads to thermal equilibrium of electrons and holes within their bands and the establishment of quasi-Fermi levels in each band. In addition, due to conversation of electric charge, the spatial density of electrons and holes is approximately the same, which permits treating

the charge carriers as a system of (neutral) excitons with characteristic densities or effective Fermi levels.

In order to explore a possible correlation between the measured DOLP values and state filling effects, we established the exciton Fermi level and effective exciton temperature based on the PL measurements. The measured integrated PL intensity at a given spectral line is proportional to the transition probability and the occupation probability of the corresponding states, at a given excitation power. The transition probability can be extracted from our numerical modeling, the state occupation probabilities can be estimated from the PL measurements. By polarization resolved PL measurements we filter out HH spectra part, since it's polarized perpendicular to the QD symmetry axis. Determination of the occupation probabilities of the state corresponding to transition then yields the corresponding quasi Fermi energies E_μ and the carrier temperature T via the relation for the Fermi-Dirac distribution: $n_{i(T)} = \frac{1}{1+e^{\frac{E_i - E_\mu}{kT}}}$

This approach is illustrated here for the case of the 240 nm PQD sample. It is applied to the side view PL spectra polarized in the growth direction, which removes the contribution of the HH-related transitions and leaves only the LH components of the VB states involved. We employed a series of PL spectra acquired at different pumping power (as in figure 10), in particular up to the stage when the GS is fully occupied (occupation probability ~1). This stage of pumping power can be estimated when by saturation of the intensity of e given spectra line. At this point of maximum GS occupation, using the ratio of calculated transition rates of the different transitions to the GS, we can deduce the occupation probabilities of the excited state transitions using this empirical formula: $n_i = \frac{Line_{Intensity}}{GS_{Intensity} \bullet J_i}$, where J_i is calculated normalized (to the GS) transition probability for particular line. Extracted states occupation probabilities found with this procedure are presented in figure 12 (a) as a function of the excitation power for the three lowest energy transitions of sample PQD-240nm. With the help of the simulated CB and VB state energies (E_i), using simple regression methods we then extract the corresponding exciton Fermi energies in figure 12 (b) and exciton temperatures in figure 12 (c). Fermi's energy level has a quadratic dependence on the excitation power and with minimum at the band edge energy. The effective carrier temperature at low excitation power is equal to the lattice temperature.

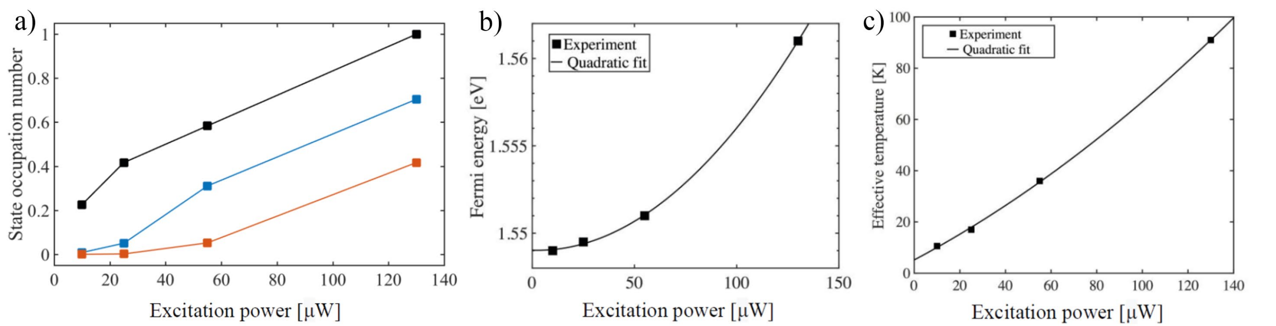

Figure 12. (a) Excitonic state occupation probability *versus excitation power for the 240 nm PQD. Black: GS, blue: first exited transition, red: second excited transition. (b) Extracted Fermi energy and (c) effective carrier temperature as a function of the excitation power. Lattice temperature is T=10 K. Solid lines in (b) and (c) are parabolic fits of the data.*

As a result, we can reconstruct calculated spectra taking into account extracted occupation probability of each state. Figure 13 displayed calculated spectra, including the state's occupation probabilities (left side). Blue and red curves correspond to different polarizations as in previous pictures. Now we can simulate power-dependent spectra and their DOLP. A comparison of the resulting DOLP (black curve) obtained in the experiment (gray) is presented on the right side of figure 12. As we see, the updated DOLP prediction fits experimental data well, even in single particle approximation, which serves as proof of our concept.

Using the approach described above, we calculated the optical spectra for several excitation levels, taking into account the extracted occupation probability of each state extracted from experimental data. The resulting calculated spectra are shown in Fig. 13 for the 240nm-PQD sample (left panels). The extracted DOLP spectra are compared with the experimental measurements on the right column of Fig. 13. There are some differences in calculated and simulated spectra's for example low energy tail which well seen for the GS, the origin of such tails is multiexciton states. The difference in spectra shapes can be explained by the fact that in our model we do not consider multiexciton states and charged excitons.

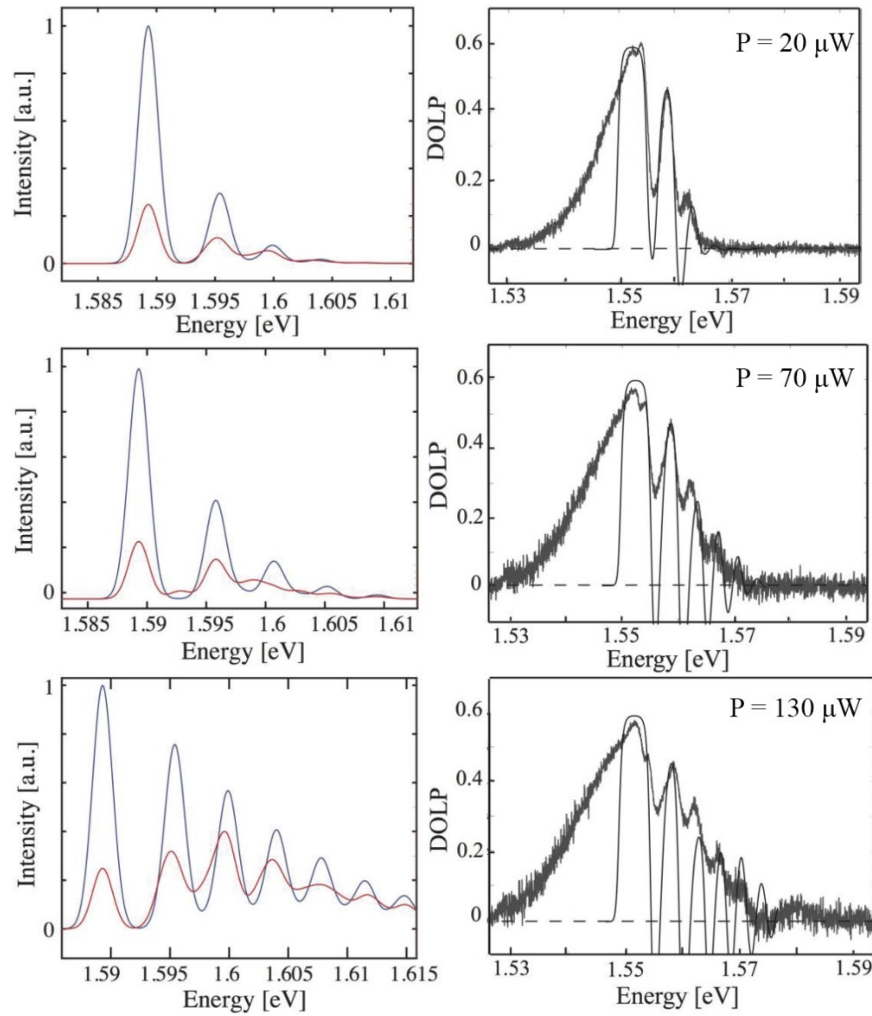

Figure 13. Comparison of calculated and experimental spectra of the 240 nm PQD structure at different excitation levels. Left column: calculated optical spectra for vertical (blue) and horizontal (red) polarizations. Right column: measured DOLP spectra (thick lines) and simulated

DOLP spectra (thin lines). Coulomb interaction as a perturbation and line broadening of 2 meV were included.

VI. Conclusion

We have investigated experimentally the theoretically the optical polarization properties of parabolically shaped QDs with different potential gradient, and compared them with those of thin QDs and long QWR structures. The investigation was performed using the same generic nanostructures realized in inverted pyramids, which allows a meaningful comparison of the effect of quantum confinement on the optical properties. The theoretical model was based on calculations of the CB-VB transitions using a detailed, realistic model of the confinement heterostructure. We concluded that VB mixing alone cannot account for the observed optical polarization anisotropy observed. However, by adding the effects of transition line broadening and state filling at different excitation level, satisfactory explanation of the optical spectra was achieved. The additional understanding on the origins of optical polarization anisotropy this gain is useful also for the design of optoelectronic devices that rely on such quantum confined structures, e.g., low dimensional lasers and sources of non-classical light.

VII. Acknowledgment

This work was supported by the Swiss National Science Foundation. All results were obtained and analyzed during PhD project at Laboratory of Physics of Nanostructures Ecole Polytechnique Fédérale de Lausanne (EPFL), Switzerland. Our acknowledgments go to Prof. Fredrik Karlsson for providing numerical codes.

VIII. References:

[1] C. F. Klingshirn, *Semiconductor Optics*. Springer, 2006.

[2] M. G. Õ. Al and N. Ga, "In-plane polarization anisotropy of the spontaneous emission of M -plane GaN / (Al , Ga) N quantum wells In-plane polarization anisotropy of the spontaneous emission" vol. 3343, no. July 2000, pp. 19–22, 2003.

[3] Q. Zhu, K. F. Karlsson, E. Pelucchi, and E. Kapon, "Transition from two-dimensional to three-dimensional quantum confinement in semiconductor quantum wires/quantum dots" *Nano Lett.*, vol. 7, no. 8, pp. 2227–2233, 2007, doi: 10.1021/nl0706650.

[4] F. Vouilloz, D. Y. Oberli, M. A. Dupertuis, A. Gustafsson, F. Reinhardt, and E. Kapon, "Polarization anisotropy and valence band mixing in semiconductor Quantum wires" *Phys. Rev. Lett.*, vol. 78, no. 8, pp. 1580–1583, 1997, doi: 10.1103/PhysRevLett.78.1580.

[5] K. F. Karlsson *et al.*, "Optical polarization anisotropy and hole states in pyramidal quantum dots" *Appl. Phys. Lett.*, vol. 89, no. 25, 2006, doi: 10.1063/1.2402241.

[6] F. Vouilloz, D. Oberli, M. Dupertuis, A. Gustafsson, F. Reinhardt, and E. Kapon, "Effect of lateral confinement on valence-band mixing and polarization anisotropy in quantum wires" *Phys. Rev. B - Condens. Matter Mater. Phys.*, vol. 57, no. 19, pp. 12378–12387, 1998, doi: 10.1103/PhysRevB.57.12378.

[7] P. Senellart, G. Solomon, and A. White, "High-performance semiconductor quantum-dot single-photon sources" *Nat. Nanotechnol.*, vol. 12, no. 11, pp. 1026–1039, 2017, doi: 10.1038/nnano.2017.218.

[8] Y. H. Huo *et al.*, "A light-hole exciton in a quantum dot" *Nat. Phys.*, vol. 10, no. 1, pp. 46–51, 2013, doi: 10.1038/nphys2799.

[9] J. He *et al.*, "Growth, Structural, and Optical Properties of Self-Assembled (In,Ga)As Quantum Posts on GaAs," doi: 10.1021/nl070132r.

[10] T. Kaizu, Y. Tajiri, and T. Kita, "Wide-wavelength-range control of photoluminescence polarization in closely stacked inas/gaas quantum dots" *J. Appl. Phys.*, vol. 125, no. 23, 2019, doi: 10.1063/1.5096411.

[11] B. Dwir, K. Leifer, and E. Kapon, "Mixed dimensionality quantum heterostructures grown in axially modulated V grooves" *Phys. Rev. B*, vol. 2121, no. 73, 2003, doi: 10.1103/PhysRevB.67.075302.

[12] A. R. Goñi, L. N. Pfeiffer, K. W. West, A. Pinczuk, H. U. Baranger, and H. L. Stormer, "Observation of quantum wire formation at intersecting quantum wells" *Appl. Phys. Lett.*, vol. 61, no. 16, pp. 1956–1958, 1992, doi: 10.1063/1.108375.

[13] H. Akiyama, "One-dimensional excitons in GaAs quantum wires" *J. Phys. Condens. Matter*, vol. 10, no. 14, pp. 3095–3139, 1998, doi: 10.1088/0953-8984/10/14/004.

[14] Q. Zhu *et al.*, "Pyramidal GaAs/ Alz Ga1-z As quantum wire/dot systems with controlled heterostructure potential" *Phys. Rev. B - Condens. Matter Mater. Phys.*, vol. 82, no. 16, pp. 1–13, 2010, doi: 10.1103/PhysRevB.82.165315.

[15] K. F. Karlsson *et al.*, "Optical polarization anisotropy and hole states in pyramidal quantum dots" *Appl. Phys. Lett.*, vol. 89, no. 25, 2006, doi: 10.1063/1.2402241.

[16] A. Hartmann, Y. Ducommun, K. Leifer, and E. Kapon, "Structure and optical properties of semiconductor quantum nanostructures self-formed in inverted tetrahedral pyramids" *J. Phys. Condens. Matter*, vol. 11, no. 31, pp. 5901–5915, 1999, doi: 10.1088/0953-8984/11/31/302.

[17] J. Szeszko *et al.*, "Exciton confinement and trapping dynamics in double-graded-bandgap quantum nanowires" *Appl. Phys. Lett.*, vol. 100, no. 21, pp. 0–4, 2012, doi: 10.1063/1.4721660.

[18] Q. Zhu, E. Pelucchi, S. Dalessi, K. Leiter, M. A. Dupertuis, and E. Kapon, "Alloy segregation, quantum confinement, and carrier capture in self-ordered pyramidal quantum wires" *Nano Lett.*, vol. 6, no. 5, pp. 1036–1041, 2006, doi: 10.1021/nl060066d.

[19] V. Troncale, K. F. Karlsson, E. Pelucchi, A. Rudra, and E. Kapon, "Control of valence band states in pyramidal quantum dot-in-dot semiconductor heterostructures" *Appl. Phys. Lett.*, vol. 91, no. 24, pp. 45–48, 2007, doi: 10.1063/1.2820693.

[20] J. Szeszko, Q. Zhu, P. Gallo, A. Rudra, and E. Kapon, "Carrier capture into semiconductor quantum dots via quantum wire barriers: Localization and thermionic emission effects" *Appl. Phys. Lett.*, vol. 99, no. 9, pp. 1–4, 2011, doi: 10.1063/1.3628320.

[21] C. Jarlov, "Cavity quantum electrodynamics with systems of site-controlled quantum dots and photonic crystal cavities" *PhD thesis, EPFL*, 2016, doi: 10.5075/EPFL-THESIS-7039.

[22] A. Hartmann, Y. Ducommun, L. Loubies, K. Leifer, and E. Kapon, “Structure and photoluminescence of single AlGaAs/GaAs quantum dots grown in inverted tetrahedral pyramids” *Appl. Phys. Lett.*, vol. 73, no. 16, pp. 2322–2324, 1998, doi: 10.1063/1.121810.

[23] A. Hartmann, L. Loubies, F. Reinhardt, and E. Kapon, “Self-limiting growth of quantum dot heterostructures on nonplanar {111}B substrates” *Appl. Phys. Lett.*, vol. 71, no. 10, pp. 1314–1316, 1997, doi: 10.1063/1.119882.

[24] M. Lazarev, J. Szeszko, A. Rudra, K. F. Karlsson, and E. Kapon, “Parabolic tailored-potential quantum-wires grown in inverted pyramids” *J. Cryst. Growth*, vol. 414, pp. 196–199, 2015, doi: 10.1016/j.jcrysgro.2014.11.008.

[25] Q. Zhu, E. Pelucchi, S. Dalessi, K. Leifer, M.-A. Dupertuis, and E. Kapon, “Alloy Segregation, Quantum Confinement, and Carrier Capture in Self-Ordered Pyramidal Quantum Wires” doi: 10.1021/nl060066d.

[26] M. Lazarev, “Tailored-Potential Semiconductor Quantum Nanostructures Grown in Inverted Pyramids” 2019.

[27] Y. Ducommun, “Semiconducter quantum dots grown in inverted pyramids.” PhD thesis, EPFL, 2001.

[28] G. Biasiol, “Formation Mechanisms of Low-Dimensional Semiconductor Nanostructures Grown by OMCVD on Nonplanar Substrates” *PhD thesis, EPFL*, vol. 1859, 1998, doi: 10.5075/epfl-thesis-1859.

[29] G. Biasiol, E. Kapon, Y. Ducommun, and A. Gustafsson, “Self-ordering of quantum-wire superlattices on V-grooved substrates” vol. 57, no. 16, pp. 9416–9419, 1998.

[30] I. Vurgaftman, J. R. Meyer, and L. R. Ram-Mohan, “Band parameters for III-V compound semiconductors and their alloys” *J. Appl. Phys.*, vol. 89, no. 11 I, pp. 5815–5875, 2001, doi: 10.1063/1.1368156.

[31] R. F. Kopf, M. H. Herman, M. L. Schnoes, A. P. Perley, G. Livescu, and M. Ohring, “Band offset determination in analog graded parabolic and triangular quantum wells of GaAs/AlGaAs and GaInAs/AlInAs” *J. Appl. Phys.*, vol. 71, no. 10, pp. 5004–5011, 1992, doi: 10.1063/1.350600.

[32] W. Langbein, H. Gislason, and J. M. Hvam, “Optimization of the confinement energy of quantum-wire states in T-shaped GaAs/Al(x)Ga(1-x)As structures” *Phys. Rev. B*, vol. 54, no. 20, pp. 14595–14603, 1996, doi: 10.1103/PhysRevB.54.14595.

[33] G. Biasiol and E. Kapon, “Mechanisms of self-ordering of quantum nanostructures grown on nonplanar surfaces” *Phys. Rev. Lett.*, vol. 81, no. 14, pp. 2962–2965, 1998, doi: 10.1103/PhysRevLett.81.2962.

[34] S. L. Chuang, N. Peyghambarian, and S. Koch, “Physics of Optoelectronic Devices” *Phys. Today*, vol. 49, no. 7, pp. 62–62, 1996, doi: 10.1063/1.2807693.

[35] P. O. Löwdin, “A note on the quantum-mechanical perturbation theory,” *J. Chem. Phys.*, vol. 19, no. 11, pp. 1396–1401, 1951, doi: 10.1063/1.1748067.

[36] J. M. Luttinger, “Quantum Theory of Cyclotron Resonance in Semiconductors : General Theory” *Phys. Rev.*, vol. 102, no. 1030, 1956.

[37] J. M. Luttinger and W. Kohn, “Motion of Electrons and Holes in Perturbed Periodic

Fields” *Phys. Rev.*, vol. 97, 1955, doi: 10.1103/PhysRev.97.869.

[38] M. A. Dupertuis *et al.*, “Symmetries and the polarized optical spectra of exciton complexes in quantum dots,” *Phys. Rev. Lett.*, vol. 107, no. 12, pp. 1–5, 2011, doi: 10.1103/PhysRevLett.107.127403.

[39] G. Fishman, “Hole subbands in strained quantum-well semiconductors in [hhk] directions” *PRB*, vol. 52, 1995, Accessed: Nov. 22, 2017. [Online]. Available: https://journals.aps.org/prb/pdf/10.1103/PhysRevB.52.11132.

[40] S. A. Empedocles, R. Neuhauser, K. Shimizu, and M. G. Bawendi, “Photoluminescence from single semiconductor nanostructures” *Adv. Mater.*, vol. 11, no. 15, pp. 1243–1256, 1999, doi: 10.1002/(SICI)1521-4095(199910)11:15<1243::AID-ADMA1243>3.0.CO;2-2.

[41] P. Boucaud, K. S. Gill, J. B. Williams, M. S. Sherwin, W. V. Schoenfeld, and P. M. Petroff, “Saturation of THz-frequency intraband absorption in InAs/GaAs quantum dot molecules” *Appl. Phys. Lett.*, vol. 77, no. 4, pp. 510–512, 2000, doi: 10.1063/1.127027.